nanomaterials

MDPI

Article

Tetrametallic Au@Ag-Pd-Pt Nanozyme with Surface-Exposed Active Sites for Enhanced Catalytic Activity

Vasily G. Panferov, Nadezhda A. Byzova, Konstantin B. Shumaev, Anatoly V. Zherdev and Boris B. Dzantiev *

A.N. Bach Institute of Biochemistry, Research Center of Biotechnology of the Russian Academy of Sciences, Leninsky Prospect 33, Moscow 119071, Russia; nbyzova@inbi.ras.ru (N.A.B.); tomorov@mail.ru (K.B.S.); zherdev@inbi.ras.ru (A.V.Z.)

* Correspondence: dzantiev@inbi.ras.ru

Abstract

Metal nanoparticles (NPs) with enzyme-mimicking activities, known as nanozymes, are being actively explored for biomedical and analytical applications. Enhancing their catalytic activity and metal utilization efficiency is crucial for advancing these technologies. Here, we report an aqueous-phase, room-temperature synthesis of tetra-metallic Au@Ag-Pd-Pt NPs that exhibit superior peroxidase-like activity compared to their mono-, bi-, and trimetallic counterparts. The synthesis involves a sequential, seed-mediated approach comprising the formation of Au NP seeds, the overgrowth of a Ag shell, and the galvanic replacement of Ag with Pd and Pt ions. We systematically investigated the effects of the Au core diameter (15, 40, 55 nm), Ag precursor concentration (50–400 μM), and the Pd-to-Pt ratio on the optical and catalytic properties. By changing the particle composition, we were able to tune the absorbance maximum from 520 nm to 650 nm while maintaining high extinction coefficients (10^9–10^{10} $M^{-1}cm^{-1}$) comparable to that of the initial Au nanoparticles. Mapping of chemical element distributions in the nanoscale range confirmed a core–shell–shell architecture with surface-enriched Pd and Pt. This structure ensures the surface-exposed localization of catalytically active atoms, yielding a more than 10-fold improvement in specific peroxidase-like activity while utilizing up to two orders of magnitude less Pt and Pd than bimetallic particles. The synthesized NPs thus combine high catalytic activity with tunable optical properties, making them promising multifunctional labels for biosensing.

Keywords: nanozymes; galvanic replacement; catalysis; peroxidase-mimicking activity; synthesis of nanoparticles; polymetallic nanoparticles

check for updates

Academic Editors: Young-Seok Shon, Juntao Zhang, Yazhou Zhang and Jiabao Ding

Received: 4 November 2025
Revised: 28 November 2025
Accepted: 2 December 2025
Published: 4 December 2025

Citation: Panferov, V.G.; Byzova, N.A.; Shumaev, K.B.; Zherdev, A.V.; Dzantiev, B.B. Tetrametallic Au@Ag-Pd-Pt Nanozyme with Surface-Exposed Active Sites for Enhanced Catalytic Activity. *Nanomaterials* **2025**, *15*, 1833. https://doi.org/10.3390/nano15231833

Copyright: © 2025 by the authors. Licensee MDPI, Basel, Switzerland. This article is an open access article distributed under the terms and conditions of the Creative Commons Attribution (CC BY) license (https://creativecommons.org/licenses/by/4.0/).

1. Introduction

Nanoparticles that mimic the catalytic activity of enzymes, termed nanozymes, are widely utilized in biomedical and analytical fields [1–4]. They are often considered more stable and cost-effective alternatives to natural enzymes and possess unique properties not found in their biological counterparts, such as localized surface plasmon resonance, magnetism, and tunable catalytic activities [5]. While these properties are advantageous, the catalytic activity, defined by parameters like turnover number and specific activity, remains the most critical characteristic [6]. However, the catalytic activity of nanozymes is often lower than that of natural enzymes, making the development of strategies to enhance it a primary focus in nanozymology.

A common strategy for increasing nanozyme activity is to maximize the number of accessible active sites [7]. In conventional spherical nanoparticles larger than 20 nm, over

90% of atoms are buried within the bulk and do not participate in catalysis. In contrast, enzymes achieve extraordinary efficiency by concentrating metal ions in exposed active sites [8]. Inspired by this, the field of single-atom catalysts has emerged [9]. Although these systems offer high atom utilization, their complex synthesis and low operational stability often limit their practical application. For conventional nanozymes, maximizing active sites can be achieved by altering the nanoparticle morphology (e.g., creating nanorods or 2D sheets) or by depositing a thin layer of catalytically active material onto a carrier particle [1]. For instance, Xia's group demonstrated that ultra-slow precursor addition can control surface deposition and diffusion [10], leading to significant activity enhancements in core@shell nanostructures, though this approach has been limited to two-component systems such as Pd-Ir [11], Au-Pt [12], Au-Ag [13] and Pd-Pt [14].

Another promising approach is to modulate the chemical composition. Multi-metallic nanoparticles often exhibit synergistic effects that boost catalytic activity beyond that of monometallic nanozymes [15]. The enhancement of catalytic activity in multi-metallic nanozymes, often termed synergy, can arise from several electronic and geometric effects [16,17]. Alloying can lead to strain effects and ligand (electronic) effects that optimize the binding energy of reaction intermediates, a key principle in heterogeneous catalysis [18]. The combination of multiple metals into a single catalyst, forming multi-metallic nanozymes, has been reported to enhance catalytic efficiency in various reactions, including the oxygen reduction reaction [19], oxygen evolution reaction [20], hydrogen evolution reaction [21], and CO oxidation [22]. The development of nanozymes that integrate multiple elements is an actively progressing research direction [23]. Several mechanisms have been proposed to explain this improved activity, such as increased surface area, mixed cation valences, a greater number of active sites, and alterations in electronic and phase structure [24]. High-entropy alloys represent a parallel development in this field [25]. The combination of multiple elements in such systems induces a lattice distortion effect, which can create sites with higher energy states conducive to catalysis, and a synergistic "cocktail" effect arising from the interaction of the various components. However, for both high-entropy alloys and multi-metallic nanozymes, the discovery of these synergistic effects and the associated improvement in catalytic activity mainly relies on an empirical trial and error approach. Therefore, the development of universal, rational synthesis strategies for multi-metallic nanozymes remains a goal of high importance.

Platinum group and noble metals (such as Au, Ag, Pd, Pt, Ir) are of particular interest due to their high intrinsic catalytic activity, chemical stability, and versatility for functionalization [26,27]. However, their high cost restricts widespread application and sharply underscores the necessity of maximizing metal utilization efficiency in catalysis [28]. Recently, nanozymes with more than three metallic elements, inspired by high-entropy alloys, have been reported [29]. However, their synthesis typically relies on complex, multistep procedures involving high temperatures, restricting their preparation to well-equipped, specialized laboratories. Moreover, the challenge of integrating multiple metals with high atom utilization in a single nanostructure remains largely unaddressed. Conventional overgrowth and co-reduction methods for synthesizing multi-metallic NPs inherently bury the most catalytically valuable metals within the core, resulting in poor atom utilization efficiency [30].

This work combines the principles of surface-exposed active sites and multi-metallic synergy through the design of tetra-metallic NPs, synthesized in aqueous phase, featuring a Au core and a Ag shell with Pd and Pt atoms. Pd and Pt atoms were introduced by galvanic replacement, so that they were located in surface-exposed areas and not buried inside particles as typically observed for conventional overgrowth methods. We demonstrate that the size, optical properties, and catalytic performance of these NPs can be tuned by

varying precursor concentrations, and we observed a systematic increase in peroxidase-like activity through the series of bimetallic (Au@Ag), trimetallic (Au@Ag-Pd) and tetra-metallic (Au@Ag-Pd-Pt) NPs.

2. Materials and Methods

2.1. Materials

$HAuCl_4$, $AgNO_3$, Na_2PtCl_6, trisodium citrate, L-ascorbic acid sodium salt, polyvinylpyrrolidone (PVP, MW 30,000), hydrogen peroxide (H_2O_2, 30%), and 3,3′,5,5′-tetramethylbenzidine (TMB) were purchased from Sigma-Aldrich (St. Louis, MO, USA). Na_2PdCl_4 was obtained from the Tokyo Chemical Industry (Tokyo, Japan). All solutions were prepared using MilliQ water (Millipore Corporation, Burlington, MA, USA).

2.2. Synthesis of Au NPs

Au NPs were synthesized via the citrate reduction of $HAuCl_4$ according to the method developed by Frens [31]. Briefly, 95 mL of deionized water was combined with 1 mL of a 1% (*w*/*v*) $HAuCl_4$ solution in a round-bottom flask equipped with a reflux condenser and heated to boiling. Under vigorous stirring, 4 mL of a 1% (*w*/*v*) trisodium citrate solution was rapidly injected. The solution was boiled for 30 min. The final size of the Au NPs was controlled by varying the volume of the 1% trisodium citrate solution added to a fixed 100 mL total reaction volume (4 mL for 15 nm, 1.5 mL for 40 nm, and 1 mL for 55 nm particles). The molar concentrations of the resulting Au NPs are reported in Table S1.

2.3. Synthesis of Au@Ag NPs

Au@Ag core–shell NPs were prepared by the ascorbate-mediated reduction of $AgNO_3$ onto the Au NP seeds [32]. First, the as-synthesized Au NPs were purified by centrifugation (17,000× *g*, 15 min) and pellets were redispersed in an equal volume of water. All subsequent steps were performed on ice using pre-cooled (4 °C) solutions to ensure uniform shell growth and prevent aggregation. For a typical synthesis, 4 mL of Au NPs was mixed with 125 µL of sodium ascorbate (50 mM) and stirred rapidly for 1 min. Then, 375 µL of a freshly prepared $AgNO_3$ solution (concentrated 12-fold relative to the desired final concentration) was added manually at a controlled rate of 100 µL/min. The reaction was allowed to proceed for 30 min on ice with continuous stirring.

2.4. Synthesis of Au@Ag-Pd-Pt

The Au@Ag NPs were incubated with 0.1% (*w*/*v*) PVP for 30 min. The PVP-coated NPs were then centrifuged and redispersed in an equal volume of water. For the galvanic replacement reaction, 600 µL of the purified Au@Ag NPs was mixed with 100 µL of freshly prepared solutions of Na_2PdCl_4 and Na_2PtCl_6. The concentrations of the Pd and Pt precursors were calculated based on the stoichiometry of the galvanic replacement reactions, where the deposition of one Pd atom requires the oxidation of two Ag atoms, and the deposition of one Pt atom requires the oxidation of four Ag atoms.

2.5. Characterization of NPs

The size and morphology of the nanoparticles were characterized using transmission electron microscopy (TEM) on a Jeol CX-100 (Jeol, Tokyo, Japan) and a Tecnai Osiris FEI microscopes (Hillsboro, OR, USA). Elemental composition and mapping were performed using energy-dispersive X-ray spectroscopy on the Tecnai Osiris FEI. UV-Vis spectra were recorded using either a Biochrom Libra S80 (Cambridge, UK) cuvette spectrophotometer or a CLARIOstar microplate reader (Offenburg, Germany). Kinetic measurements of peroxidase-like activity and the calculation of Michaelis–Menten constants and specific ac-

tivities were conducted according to the procedures detailed in our previous work [32]. The peroxidase-like kinetics were characterized using the $Au_{55nm}Ag_{200\mu M}Pd_{50\%}Pt_{50\%}$ nanoparticles (140 µg/mL). The nanoparticles were incubated with a solution containing 0.5 mM TMB and varying concentrations of H_2O_2 (0–3000 mM) in 20 mM sodium acetate buffer (pH 4.0). The kinetics of TMB oxidation were monitored by the increase in absorbance at 650 nm for 2 min. The initial reaction rate was determined from the linear slope within the first 40–60 s. Specific peroxidase-like activity was determined according to the method described by Jiang et al. [33]. Serial dilutions of NPs were incubated with a substrate solution containing 0.5 mM TMB and 1500 mM H_2O_2 in 20 mM sodium acetate buffer (pH 4.0). The initial rates were calculated and converted into the rate of TMB oxidation (µM/s) using the molar extinction coefficient for oxidized TMB (ε_{650} = 39,000 M^{-1} cm^{-1}). Formation of hydroxyl radicals was monitored by electron paramagnetic resonance (EPR). 5,5-Dimethyl-1-pyrroline N-oxide (DMPO) was used as a spin trap. EPR spectra were measured at ambient temperature (25 °C) using an X-band EPR spectrometer E-109E (Varian, USA). The instrument settings were as follows: modulation frequency, 100 kHz; time constant, 0.032; microwave power, 10 mW; microwave frequency, 9.15 GHz; and modulation amplitudes: 0.1 mT for DMPO spin adducts. For the assay, $Au_{60nm}Ag_{400\mu M}Pd_{20\%}Pt_{40\%}$ nanoparticles (1 µg/mL) were mixed with freshly prepared 55 mM DMPO and 150 mM H_2O_2, followed by a 5 min incubation. A Fenton reaction induced by 0.5 mM $FeSO_4$ served as a positive control.

3. Results

3.1. General Strategy

The synthesis of tetra-metallic nanoparticles involved sequential stages: (1) synthesis of spherical Au nanoparticle seeds, (2) formation of a Ag shell over the Au seeds to form Au@Ag core–shell nanoparticles, and (3) partial galvanic replacement of the Ag shell with Pd and Pt by introducing $PdCl_4^{2-}$ and $PtCl_6^{2-}$ ions (Figure 1). We utilized three different diameters of Au seeds (15, 40 and 55 nm) to investigate the effect of core size. This variation not only changes the total surface area available for Ag deposition but also, for a fixed mass concentration of gold, inversely affects the number of seed particles (Table S1). Consequently, these factors collectively influence the ultimate thickness of the Ag shell and the loading of Pd and Pt atoms per individual nanoparticle.

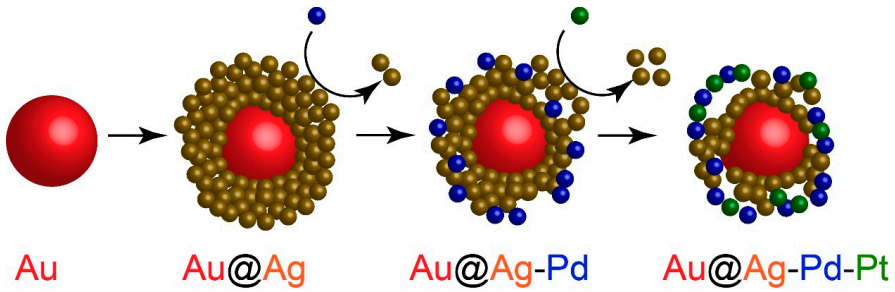


Figure 1. Schematics of NP synthesis.

The silver shell was formed by reducing silver nitrate with sodium ascorbate in the presence of the Au NP seeds. To ensure the formation of a uniform and smooth shell, the reaction was carried out at a low temperature with a controlled, slow addition of the silver nitrate precursor at a rate of 100 µL/min. Using this method, a total of 12 distinct Au@Ag core–shell samples were synthesized. This library was generated by systematically varying two parameters: the core size (15, 40, and 55 nm) and the concentration of silver nitrate precursor (50, 100, 200, and 400 µM). The samples were designated accordingly

($Au_{15nm}Ag_{50\mu M}$, $Au_{15nm}Ag_{100\mu M}$, $Au_{15nm}Ag_{200\mu M}$, and $Au_{15nm}Ag_{400\mu M}$, and similarly for Au_{40nm} and Au_{55nm}).

The silver shell functions as a sacrificial template for the galvanic deposition of Pd and Pt. Galvanic replacement is a thermodynamically driven redox process that proceeds at room temperature without requiring external reducing agents. The driving force is the difference in reduction potentials between the sacrificial metal and the depositing metal ion, where the depositing metal must have a higher standard reduction potential [34]. Silver, with its relatively low reduction potential ($Ag^+/Ag = 0.80$), is a common sacrificial template for ions like $PdCl_4^{2-}$ ($Pd^{2+}/Pd = 0.91$) [35] and $PtCl_6^{2-}$ ($Pt^{4+}/Pt = 1.18$) [34]. While powerful, the application of galvanic replacement has been largely confined to bimetallic systems [36]. In this work, we extended it to create tri- and tetra-metallic nanostructures. The process was performed in two sequential steps: First, we performed the addition of $PdCl_4^{2-}$ ions to Au@Ag particles to form trimetallic Au@Ag-Pd NPs, followed by the addition of $PtCl_6^{2-}$ ions to yield the final tetra-metallic Au@Ag-Pd-Pt NPs. We confirmed that the sequence of ion addition ($PdCl_4^{2-}$ before $PtCl_6^{2-}$ or vice versa) had no significant effect on morphology and catalytic activity of the final product (Figure S1), although an excessive concentration of $PtCl_6^{2-}$ was avoided to prevent the potential replacement of previously deposited Pd.

The stoichiometry of the reaction dictates the final morphology. The reduction of one Pd atom (from $PdCl_4^{2-}$) requires the oxidation of two Ag atoms, while the reduction of one Pt atom (from $PtCl_6^{2-}$) requires four Ag atoms. Because the number of oxidized Ag atoms exceeds the number of deposited Pd or Pt atoms, the process leads to the formation of porous, cage-like structures with internal voids [37]. This mechanism ensures that the deposited Pd and Pt atoms are directly surface-exposed, rather than buried, making galvanic replacement an ideal strategy for maximizing atom utilization efficiency [32]. To prevent the precipitation of nanoparticles by AgCl, which forms from the Ag^+ ions released during the reaction, the Au@Ag nanoparticles were stabilized with a coating of polyvinylpyrrolidone (PVP) prior to galvanic replacement. Au@Ag particles capped with PVP were centrifuged and redispersed in H_2O to remove free PVP. The excess of free PVP could complex with the Pt and Pd precursors [38], affecting their reactivity. Potentially, alternative non-halide complexes of Pd and Pt could be used to avoid the precipitation of poorly soluble AgCl. However, most current protocols utilize chloride precursors and instead employ various methods to remove the formed AgCl, such as treatment with ammonium hydroxide [39], HCl/NaCl washing [40,41] or heating [42].

Based on the stoichiometry of the galvanic replacement reactions, we denote our NPs to reflect the percentage of the maximum possible Pd and Pt deposition, as determined by the available Ag. For example, a sample named $Au_{55nm}Ag_{200\mu M}Pd_{50\%}Pt_{50\%}$ indicates that 50% of the sacrificial Ag was replaced by Pd deposition and 50% by Pt. To establish general trends, we studied the effect of multiple variables, including Au core size, Ag shell thickness, and Pd/Pt ratio, on the morphology, optical properties, and catalytic activity of the resulting NPs. Given that the total number of synthesized NPs exceeded 60, key composition–property relationships were established using a selected set of preparations that effectively represented the entire parameter space. This approach allowed us to generalize our conclusions and establish robust trends linking composition to morphology and, ultimately, to functional properties.

3.2. Characterization of the Morphology of NPs

The spherical Au nanoparticles synthesized as seeds were characterized by transmission electron microscopy (TEM). As shown in Figure 2a, the particles were monodisperse and largely spherical with no observable aggregation, confirming their suitability for subse-

quent seed-mediated growth. The mean diameters were determined to be 15.9 ± 1.2 nm, 40.6 ± 5.5 nm, and 53.3 ± 4.0 nm. These are referred to throughout the text as Au_{15nm}, Au_{40nm}, and Au_{55nm}, respectively.

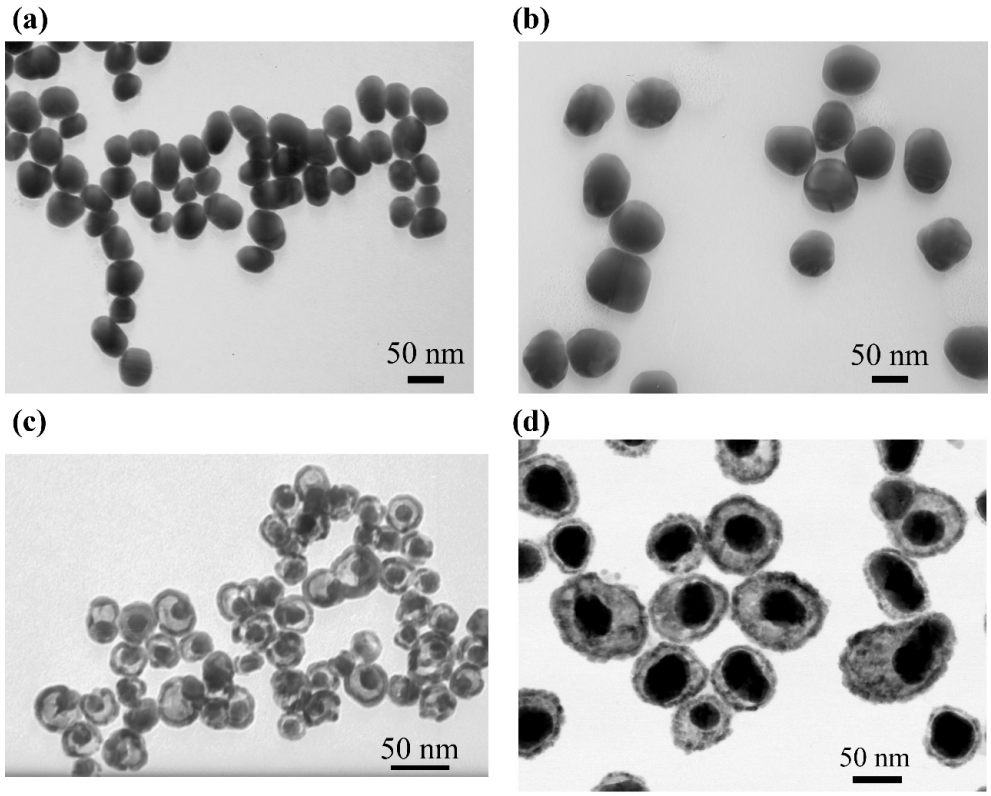


Figure 2. TEM of NPs. (**a**) Au_{55nm} NPs. (**b**) $Au_{55nm}Ag_{400\mu M}$. (**c**) $Au_{15nm}Ag_{100\mu M}Pd_{50}$. (**d**) $Au_{40nm}Ag_{400\mu M}Pd_{25}Pt_{40}$.

TEM analysis of the Au@Ag nanoparticles confirmed high monodispersity and a notable absence of aggregates (Figure 2b and Figure S2). Maintaining a low temperature during synthesis was critical, as elevated temperatures often lead to the "soldering" of Au cores, particularly at high silver nitrate concentrations. The optimized conditions employed here successfully prevented such aggregation, cross-linking, and homogeneous nucleation of free-standing Ag NPs. The final size of the Au@Ag NPs exhibited a clear correlation with both the concentration of silver nitrate and the diameter of the initial Au seeds. For instance, using 15 nm Au seeds, the mean diameter increased from 18.0 ± 1.8 nm (at 100 μM $AgNO_3$) to 25.1 ± 2.3 nm (at 400 μM $AgNO_3$), confirming tunable and controlled overgrowth. Due to differences in the total surface area and population density of the seed particles, the resulting Ag shell thickness varied for Au_{15nm}, Au_{40nm}, and Au_{55nm} seeds even at identical silver nitrate concentrations.

Both the trimetallic (Au@Ag-Pd) and tetra-metallic (Au@Ag-Pd-Pt) NPs displayed the characteristic porous and cage-like morphology indicative of galvanic replacement (Figure 2c,d). Given that their synthesis shares the same underlying mechanism, a similar morphology is expected. This structural evolution is a direct consequence of the process stoichiometry, wherein a greater number of Ag atoms are oxidized and removed than the number of Pd or Pt atoms deposited. Furthermore, the larger atomic radius of Ag and its face-centered cubic lattice constant compared to Pd and Pt contribute to the formation of these porous frameworks with regions of low electron density.

3.3. Characterization of Composition of NPs

While TEM effectively visualized the morphological changes, it cannot confirm the co-deposition of Pd and Pt. To verify the successful formation of tetra-metallic NPs, energy-dispersive X-ray spectroscopy (EDS) was performed. The EDS spectrum (Figure 3a) confirmed the presence of all four metallic elements (Au, Ag, Pd, Pt), with the signals for Pd and Pt being relatively lower, as anticipated given their surface-limited deposition. The detection of chlorine is consistent with the precipitation of AgCl from Ag^+ ions released during galvanic replacement. To probe the elemental distribution, EDS line scanning and elemental mapping were employed. The line profile (Figure 3b) is characteristic of a core–shell structure, showing a Ag shell surrounding the Au core. The profiles for Pd and Pt were distributed across the entire particle, consistent with their deposition throughout the porous cage. This was confirmed by TEM-EDS elemental mapping (Figure 3c–e), which clearly visualized the localization of all four elements within a single nanoparticle. The maps show the Au core surrounded by a Ag shell, with both Pd and Pt elements scattered across the edges and surface of the structure, aligning perfectly with the expected model (Figure 1).

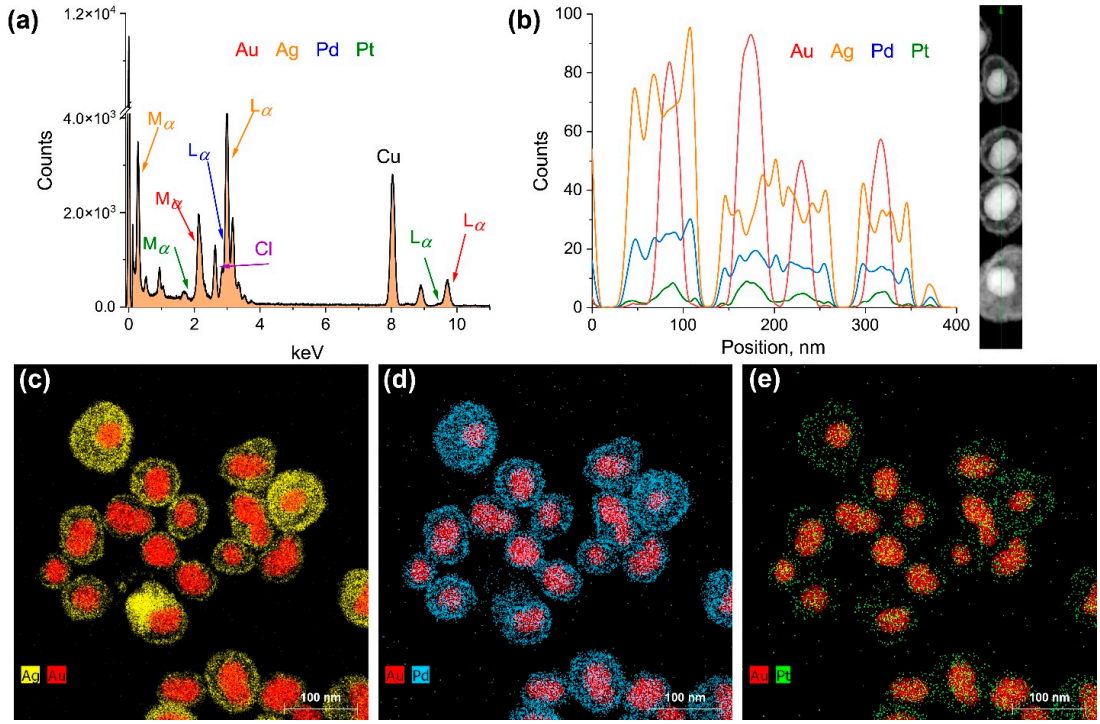


Figure 3. Characterization of chemical composition of $Au_{40nm}Ag_{400\mu M}Pd_{40\%}Pt_{40\%}$. (**a**) EDS spectrum confirming the presence of Au, Ag, Pd, and Pt. (**b**) EDS line profile across a cluster of nanoparticles, showing the distribution of elements. (**c**–**e**) TEM-EDS elemental maps of a single representative nanoparticle: (**c**) Au (red) and Ag (yellow), (**d**) Au (red) and Pd (blue), and (**e**) Au (red) and Pt (green).

The final composition of the tetra-metallic nanozymes is governed by the distinct stoichiometry of the galvanic replacement reactions. The deposition of a single Pd atom requires the oxidation of two Ag atoms, whereas the deposition of a single Pt atom requires the oxidation of four Ag atoms. Consequently, for an identical nominal percentage of precursor (e.g., 40% for both Pd and Pt in $Au_{40nm}Ag_{400\mu M}Pd_{40\%}Pt_{40\%}$, Figure 3), the resulting atomic concentration of Pd in the final nanoparticle is twice that of Pt. This is clearly demonstrated by the higher signal intensity for Pd in the compositional analysis (Figure 3d,e).

The galvanic replacement reaction occurs exclusively at the particle–solvent interface, localizing the deposited materials at surface-exposed sites. Although the initially deposited atoms can theoretically undergo interdiffusion (e.g., via the Kirkendall effect) to form alloyed structures, the interdiffusion rate of Pd is higher than that of Pt. To test this, we estimated the relative concentration of Pd at the particle edges versus the center. If our hypothesis of surface enrichment is valid, a higher Pd concentration should be found near the edges (i.e., the original Ag shell). If interdiffusion rate is sufficient, alloy articles with no enrichment of Pd at specific regions will be detected.

Quantitative EDS analysis of the atomic composition (Figure 3d) confirmed this. The relative fraction of Pd at the particle center was 12.2% ± 1.2% (with a total signal of 762 ± 30 counts/s), while the concentration near the edges was significantly higher, at 36.6% ± 6.0% (total signal 98 ± 7 counts/s). Therefore, the results from both chemical mapping (Figure 3c–e) and EDS confirm that Pd atoms remain predominantly enriched at the edges and surface. This is consistent with the expected mechanism of a surface-limited galvanic replacement process.

3.4. Characterization of the Optical Properties of NPs

The optical properties of nanozymes, particularly in the visible region, are critically important for their use as colorimetric labels. In addition, modifications of optical properties are a sensitive indicator of changes in chemical composition and morphology of NPs [43]. The initial Au NPs serve as excellent colorimetric labels due to their high molar extinction coefficient (ε). Therefore, we systematically investigated how the sequential formation of the Ag shell and the deposition of Pd and Pt atoms affect both the position of the localized surface plasmon resonance peak (λ_{max}) and the corresponding ε-values. As the absence of homogeneous nucleation was confirmed, the molar concentration of particles can be accurately estimated by the theoretical calculations of Au seed concentration (Table S1).

The overgrowth of the Ag shell onto the Au seeds resulted in a blue-shift of the localized λ_{max}, accompanied by a substantial increase in the optical density (Figure 4a). This enhancement ε-values makes Au@Ag core–shell nanoparticles even more efficient colorimetric labels than the initial Au NPs. Subsequent galvanic replacement of the sacrificial Ag shell induced a pronounced red-shift of the λ_{max} to wavelengths longer than those of the original Au NPs, coupled with a strong decrease in the optical density (Figure 4a), yielding violet-blue colloidal solutions. The deposition of Pt onto the trimetallic Au@Ag-Pd NPs did not induce further significant spectral changes. Consequently, the final λ_{max} positions of the tri- and tetra-metallic nanoparticles were similar and were predominantly determined by the size and shape of the initial Au seeds. This indicates that tailoring the Au core architecture is an effective strategy for controlling the optical properties of the resulting multi-metallic nanostructures.

The utility of nanoparticles as a colorimetric label is primarily governed by their ε-values, and maximizing this parameter is key to developing highly sensitive bioassays [44]. Our results confirm that the bimetallic Au@Ag NPs possess the highest ε values among all samples studied. Galvanic replacement led to a reduction in ε (Figure 4b). However, galvanic replacement also resulted in a broadening of the absorption peak and increased optical density at longer wavelengths (>600 nm), as seen in Figure 4a. For applications relying on bare-eye readout, such as lateral flow assays, the perceived intensity of coloration, which integrates absorption across the visible spectrum, is more critical than the absorbance at a single wavelength. To evaluate this, we quantified the total area under the extinction spectrum from 350 to 800 nm (integrated intensity), as reported by Bai et al. [45]. These results (Figure S3) revealed that the trimetallic NPs maintained integrated extinction

values comparable to the initial Au NPs, with trends similar to those observed for the molar extinction coefficient.

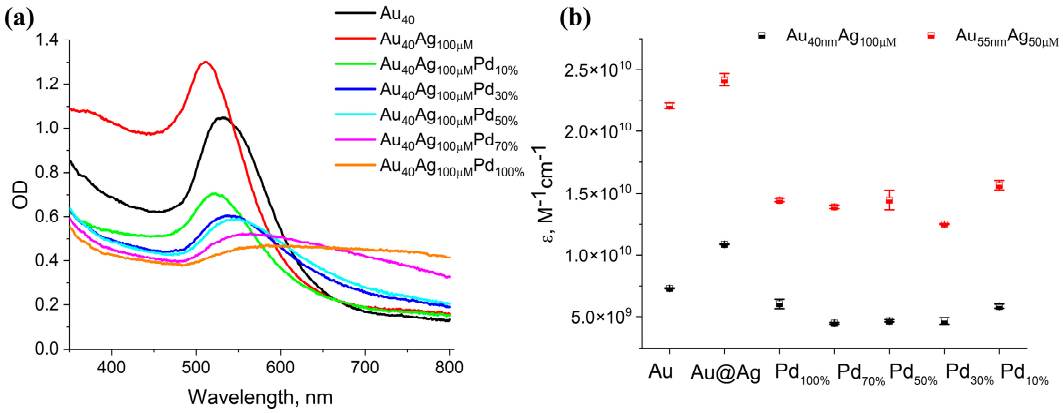


Figure 4. The effect of Pd loading on the optical properties of the nanoparticles. (**a**) UV-Vis spectra of NPs. (**b**) Molar extinction coefficients at the λ_{max} wavelength.

In summary, although the galvanic replacement process reduces the peak ε-value, the resulting tri- and tetra-metallic NPs retain remarkable optical properties, with integrated extinction performance comparable to Au NPs, which are often considered the "gold standard" for colorimetric labels. Therefore, these multifunctional nanoparticles are promising not only as catalytic nanozymes but also as intrinsic colorimetric reporters in biosensing applications.

3.5. Characterization of the Catalytic Properties of NPs

The synthesized nanoparticles exhibited intrinsic peroxidase-like activity, catalyzing the oxidation of TMB in the presence of H_2O_2. It is important to note that the AgCl precipitate that formed during galvanic replacement was found to suppress catalytic activity and turnover number (k_{cat}) (Figure S4), despite having no effect on the optical properties. For some nanoparticles (e.g., $Au_{40nm}Ag_{100\mu m}Pd_{100\%}$, Table S2), the lack of a AgCl removal step resulted in particle aggregation of particles and a consequent dramatic reduction in catalytic activity. Therefore, prior to all catalytic assays, NPs were treated with ammonium hydroxide (NH_4OH, 10 mM) to dissolve AgCl [39], followed by multiple rounds of centrifugation to remove dissolved species and ensure the removal of the alkaline solution. EDS demonstrated a significant reduction in the peak at 2.62 keV after treatment with NH_4OH (Figure S5A). This peak corresponds to the Kα emission line of chlorine, confirming the effective dissolution of AgCl. Because the AgCl layer was thin, no changes in nanoparticle morphology were observed (Figure S5B,C).

We confirmed that the bi-, tri-, and tetra-metallic nanoparticles exhibit peroxidase-like activity, which qualifies them as nanozymes. It is important to note that all nanozymes used in this study were coated with PVP, which partially blocks the catalytic surface, resulting in reduced catalytic activity [46]. However, synthesis without the PVP capping agent often resulted in excessive aggregation. Therefore, despite the cost of reduced activity, we used only PVP-coated particles to ensure colloidal stability. For instance, the aggregated $Au_{40nm}Ag_{100\mu m}Pd_{100\%}$ demonstrated more than 27-times lower k_{cat} value compared to the non-aggregated particles (Table S2).

Kinetic analysis of TMB oxidation revealed a Michaelis–Menten constant (K_M) for H_2O_2 of 320 ± 20 μM (Figure 5a). The oxidase-like activity (TMB oxidation in the absence of H_2O_2) of the particles was negligible. While the Au@Ag core–shell NPs themselves possessed moderate peroxidase-like activity, we focused on the enhancement provided by the deposition of Pd and Pt. The effect was studied using $Au_{40nm}Ag_{100\mu M}$ and $Au_{40nm}Ag_{200\mu M}$.

In total, eight NPs particles with various Pd and/or Pt loads ($Pd_{10\%}$, $Pd_{10\%}Pt_{15\%}$, $Pd_{50\%}$, $Pd_{50\%}Pt_{8\%}$ for each type of Au@Ag) were prepared and used for kinetic measurements. The initial rates of TMB oxidation were higher for the tetra-metallic (Au@Ag-Pd-Pt) NPs compared to their trimetallic (Au@Ag-Pd) counterparts (Figure 5b). For a more quantitative comparison, we calculated k_{cat} for selected NPs. The calculations were based on the total molar concentration of nanoparticles (recalculated from the concentration of Au seeds), an approach that typically underestimates the absolute activity but allows for a valid comparative analysis between different nanostructures [47,48]. However, this recalculation (based on the molar concentration of nanoparticles) is highly relevant for bioanalytical applications where the analytical signal originates from nanozyme-labeled complexes, such as in a nanozyme–antibody–antigen conjugate [6]. The initial rates of TMB oxidation (Figure 5b) for 14 various tri- and tetra-metallic nanozymes were calculated from kinetic curves at saturating H_2O_2 concentrations (2000 mM). The values of k_{cat} (Table S2) were determined as the ratio of the reaction rate (nM/s) to the molar concentration of particles (nM). The results (Figure 5c) demonstrate that the galvanic deposition of Pt significantly boosted the catalytic efficiency. For instance, adding 15% Pt to the $Au_{40nm}Ag_{100\mu M}Pd_{10\%}$ NP resulted in an almost two-fold increase in k_{cat}. A similar improvement was observed for $Au_{40nm}Ag_{100\mu M}Pd_{50\%}$ even at a lower Pt load (8%). Comparable improvements in k_{cat} (2.2-fold for $Pd_{10\%}Pt_{15\%}$ and 1.5-fold for $Pd_{50\%}Pt_{8\%}$, Figure 5d) were observed for $Au_{40nm}Ag_{200\mu M}$ NPs, which confirms that tetra-metallic NPs are more efficient peroxidase-like nanozymes.

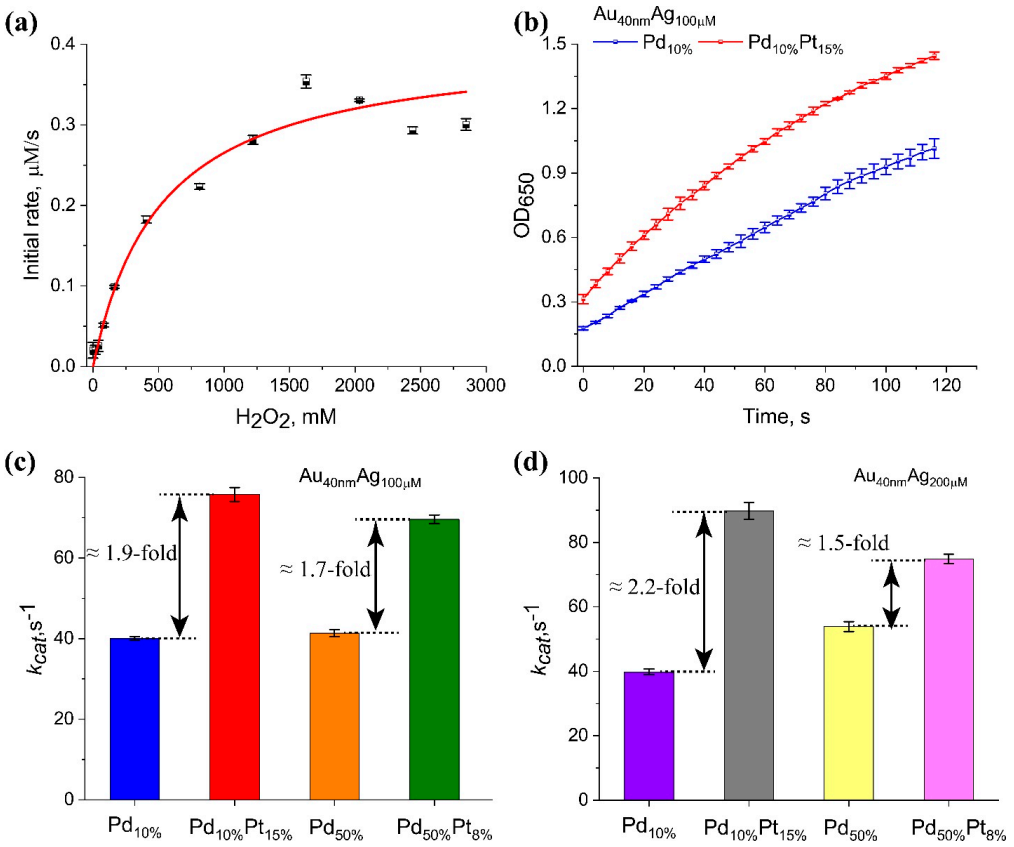


Figure 5. Peroxidase-like catalytic activity of NPs. (**a**) Michaelis–Menten kinetics of TMB oxidation for $Au_{55nm}Ag_{200\mu M}Pd_{50\%}Pt_{50\%}$ NP. (**b**) Initial reaction rates of TMB oxidation for NPs with varying Pd and Pt compositions. (**c**) k_{cat} values for $Au_{40nm}Ag_{100\mu M}$ NPs with different Pd/Pt loads. (**d**) k_{cat} values for $Au_{40nm}Ag_{200\mu M}$ NPs with different Pd/Pt loads.

Although nanozymes catalyze typical enzyme reactions, the exact mechanisms of enzyme and nanozyme catalysis typically differ [49]. Nanozymes of various compositions often generate reactive oxygen species, which determine their analytical and biomedical applications [50]. Hydroxyl radicals are among the most commonly reported reactive oxygen species generated by nanozymes [51], and peroxidase-like oxidation of substrates is generally associated with the generation of these radicals [52]. We confirmed that $Au_{60nm}Ag_{400\mu M}Pd_{20\%}Pt_{40\%}$ generates hydroxyl radicals (Figure S6), which are able to oxidize TMB.

To establish general composition–activity relationships, we evaluated a broad panel of twenty NPs based on the Au_{55nm} core with varying Ag shell thicknesses (50–400 µM $AgNO_3$) and Pd/Pt ratios. The specific activity (activity per mass of catalyst) was used as the quantitative parameter for this high-throughput screening (Figure 6a). The mass of the core–shell particles was calculated based on the mass of the Au seeds. This is a reliable approach, as no homogeneous nucleation (i.e., the formation of standalone Ag-Pd-Pt particles not grown on Au seeds) was detected. The initial rates of TMB oxidation were first determined using various mass loads of the nanozymes (Figure 6a). Nanozyme activity was quantified from the initial rates ($\Delta OD_{650}/\Delta t$), derived from the linear regions of the kinetic plots ($R^2 \geq 0.98$, shown as lines in Figure 6a). One unit of nanozyme activity (U) was defined as the amount of nanozyme required to oxidize 1 µM of substrate per minute under the specified conditions. Consistent with the Michaelis–Menten kinetic model, the reaction rate showed a linear relationship with the amount of catalyst. Subsequently, the initial rates were plotted against the mass of particles (Figure 6b), and the slope of this line was defined as the specific activity of the nanozyme (U/mg). The resulting data of specific activity (Figure 6c) provide clear insights into the synergistic effects of the Ag shell thickness and the Pd/Pt loading ratio on the peroxidase-mimicking activity.

Deposition of a low concentration of Pd ($Pd_{10\%}$) onto Au@Ag cores resulted in a 2–3.5-times increase in specific peroxidase activity (Figure 6c). A further increase in Pd load ($Pd_{50\%}$) provided a relatively moderate 1.1–1.5-times increased activity compared to trimetallic particles with $Pt_{10\%}$ loads, while improving the activity compared to Au@A up to 5 times. Subsequent loading of these trimetallic particles with Pt resulted in a comparable increase in specific activity, by a factor of 2–4 for $Ag_{50\mu M}Pd_{10–50\%}$ (e.g., from 1.6 to 6.3 for $Ag_{50\mu M}$ $Pd_{10\%}$, and from 2.2 to 3.7 for $Ag_{50\mu M}Pd_{50\%}$), 2–3 for $Ag_{100\mu M}Pd_{10–50\%}$, 2–2.5 for $Ag_{200\mu M}Pd_{10–50\%}$, and 2–4 for $Ag_{400\mu M}Pd_{10–50\%}$.

The fact that both sequential doping steps, first with Pd and then with Pt, yielded improvements of a similar magnitude indicates that both metals contribute significantly to the overall catalytic performance. The observed activity is therefore not primarily attributable to Pt or Pd alone, but arises from a cooperative effect. This synergy could be explained by electronic ligand effects, where the interaction between different metals at the nanoparticle surface modifies the local electronic environment, potentially optimizing the binding energy of reaction intermediates and facilitating the electron transfer processes crucial for the peroxidase-like cycle [53].

Furthermore, the activity of the tetra-metallic nanozymes aligns with previously reported values for peroxidase-mimicking nanozymes. An accurate comparison of activities is only valid for k_{cat} and specific activity values, whereas the commonly used assessment based solely on K_M and V_{max} can be misleading [47]. Although k_{cat} comparison is theoretically valid, it is often impractical due to the lack of a universally accepted definition for the nanozyme active center [54]. Therefore, we compared the specific peroxidase-mimicking activities (Figure 6c), which are normalized per milligram of catalyst, which is consistently used across the literature. As shown in Table S3, the synthesized nanozymes achieve

activity levels comparable to those reported for other systems, but with a significantly lower concentration of precursors (typically by one to two orders of magnitude).

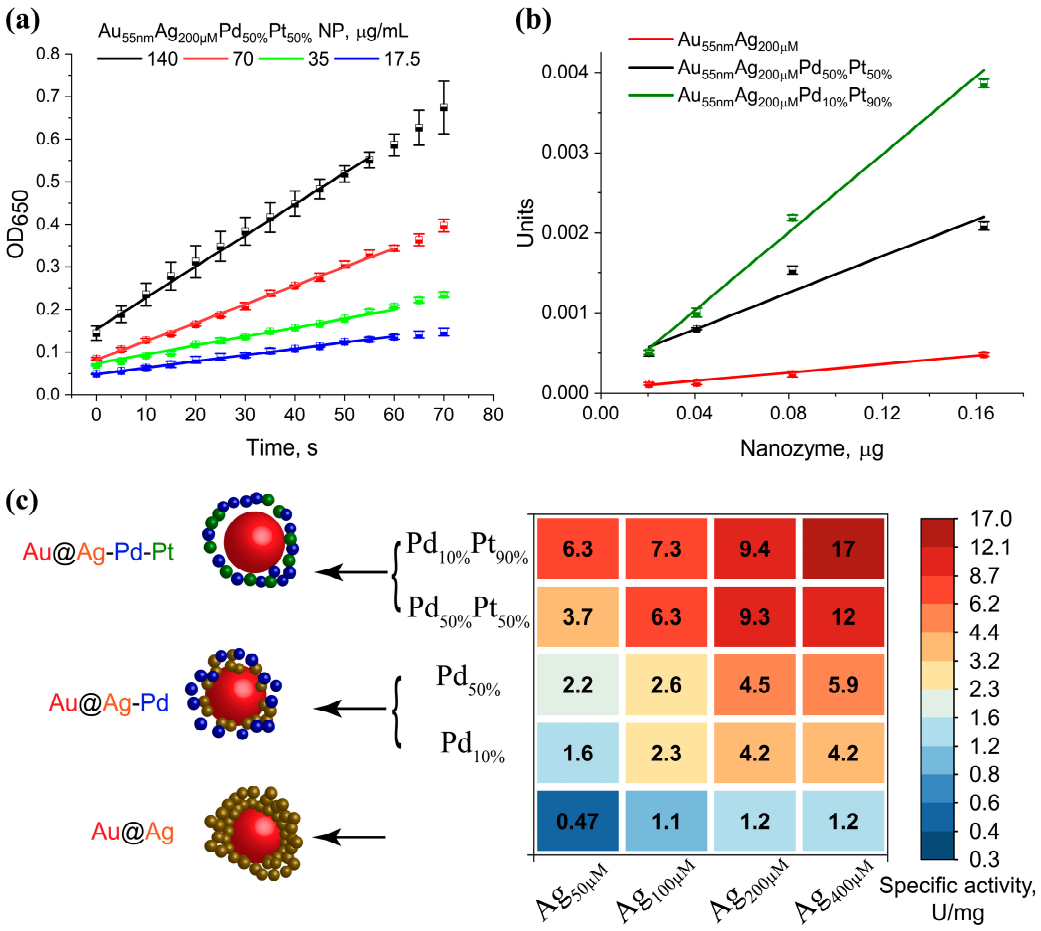


Figure 6. Specific peroxidase-like activity of tetra-metallic NPs. (**a**) Estimation of the initial rate of the reactions for various dilutions of NPs. (**b**) Effect of nanozyme amount on catalytic activity unit. (**c**) The values of specific activity of Au_{55nm}-based NPs, showing the influence of Ag shell thickness and Pd/Pt ratio.

A key finding of this study is the exceptional metal utilization efficiency achieved by the used synthetic approach. The total concentration of Pt employed in the galvanic replacement (10–50 μM) was one to two orders of magnitude lower than the amounts typically used to form bimetallic Au@Pt or Au@Pd core–shell nanoparticles. Remarkably, despite this reduction in precious metal input, the resulting tetra-metallic Au@Ag-Pd-Pt nanoparticles exhibited a specific catalytic activity that was comparable to, and often surpassed, that of their bimetallic counterparts. This underscores the synergistic advantage of the multi-metallic, surface-exposed structure. Catalysts that minimize the consumption of precious noble metals are of great interest from both economic and environmental perspectives. The synthesis approaches utilized here are designed to minimize the use of these high-cost materials while maximizing their efficiency. Noble metals are highly stable under various chemical and physical stresses, including elevated temperatures, extreme pH, and the presence of inhibitors [55,56]. While this stability is beneficial for prolonged catalyst lifetime, it also presents a significant challenge for metal recovery. As demonstrated in our recent paper, aqua regia is one of the few reagents capable of terminating the catalytic reaction and subsequently recovering Au, Pt, and Pd in their ionic forms, making them available for reuse [57]. In future work, we will focus on a detailed evaluation of the catalytic mechanism and a more accurate quantitative

analysis of the activity normalized to the mass of the catalytically active metals (Pd and Pt) to fully elucidate the metal utilization efficiency.

The tetra-metallic Au/Ag/Pd/Pt nanozymes exhibited high colloidal stability (Figure S7) and maintained their chemical composition, as verified by unchanged optical spectra (Figure S8). In contrast, as previously reported for Au@Ag nanozymes, the silver shell was oxidized by H_2O_2, indicated by a significant shift in the maximum wavelength and an obvious color change of the nanoparticle solution (Figure S8B). Furthermore, the tetra-metallic nanozymes withstood multiple cycles of substrate renewal and prolonged catalysis with no significant loss of the initial reaction rate, confirming their high operational stability.

Finally, we confirmed the reproducibility of the proposed synthesis procedure by characterizing four independent batches of the $Au_{40nm}Ag_{100\mu M}Pd_{50\%}Pt_{50\%}$ nanozyme. The hydrodynamic diameters and initial rates of TMB oxidation were highly consistent across all batches. The variation in hydrodynamic diameter was within 10% (Figure S9), confirming the high reproducibility of the synthesis. Minor differences were observed in the population of particles sized 2–20 nm, which may be attributed to residual PVP. However, the total fraction of these particles was less than 2%, further confirming synthesis robustness. More importantly, the peroxidase-mimicking activity was highly reproducible, with the initial rates varying by approximately 10% across different batches (Figure S10). This directly demonstrates the successful and consistent reproduction of the nanozyme's catalytic function.

4. Conclusions

While the relationship between composition, optical properties, and catalytic activity has been explored for bimetallic [58,59] and trimetallic [32,45] noble metal nanozymes, systems with four or more metals have not yet been systematically investigated. We have developed a robust and tunable aqueous-phase strategy for synthesizing tetra-metallic Au@Ag-Pd-Pt nanoparticles. This approach provides exceptional control over the NPs' composition, morphology, and properties. Galvanic replacement ensures that catalytically active Pd and Pt atoms are preferentially located on the nanoparticle surface, making them accessible for substrate binding. Furthermore, the multi-metallic NPs retain tunable plasmonic properties inherited from the Au core, an advantage over conventional bimetallic core@shell NPs. The combination of high catalytic activity and strong optical extinction within a single nanostructure is particularly valuable for biosensing applications. In summary, this work presents not just another new nanozyme, but a versatile synthetic platform. The principles demonstrated here can be extended to other catalytic metals (e.g., Cu, Rh, Ru, Mn) and complex compositions, opening a pathway for the synthesis of high-entropy alloy nanozymes and other functional materials.

High-activity catalysts that minimize the consumption of precious noble metals have applications extending far beyond biosensing, reaching into industrial catalysis and environmental remediation. In industrial catalysis, many processes (from fine chemical synthesis to petroleum refining) rely on catalysts containing platinum group metals [60]. The synthesis strategy demonstrated here provides a viable pathway to reduce the cost and environmental footprint of such industrial processes. In environmental remediation, these nanozymes could serve as catalysts for degrading pollutants in wastewater [61]. Furthermore, this synthetic approach aligns with the principles of green chemistry and sustainable development. The high stability and cost of noble metals also make them prime candidates for recovery and recycling.

Supplementary Materials: The following supporting information can be downloaded at https://www.mdpi.com/article/10.3390/nano15231833/s1: Table S1. Concentration of synthesized Au nanoparticle seeds; Figure S1. Effect of reagent addition order during galvanic replacement on the morphology and functional properties; Figure S2. TEM images of Au@Ag NPs; Figure S3. Integrated extinction area under the UV-Vis spectrum (350–800 nm) for various nanoparticle compositions; Figure S4. The effect of AgCl dissolution with NH_4OH on the turnover number in the peroxidase-like TMB oxidation reaction. Figure S5. Effect of NH_4OH treatment on the morphology and composition of nanozymes; Table S2. The values of k_{cat} for various nanozymes; Figure S6. EPR spectra for hydroxyl radical detection; Table S3. The values of specific peroxidase activity reported for various nanozymes; Figure S7. Hydrodynamic size distribution of nanozymes; Figure S8. Stability assessment via optical spectroscopy; Figure S9. Reproducibility of nanozyme synthesis; Figure S10. Reproducibility of nanozyme peroxidase-like activity. References [62–95] are cited in the supplementary materials.

Author Contributions: Conceptualization, V.G.P. and A.V.Z.; methodology, V.G.P. and N.A.B.; validation, V.G.P. and N.A.B.; formal analysis, A.V.Z. and B.B.D.; investigation, V.G.P., N.A.B. and K.B.S.; resources, A.V.Z. and B.B.D.; data curation, A.V.Z.; writing—original draft preparation, V.G.P., A.V.Z. and B.B.D.; writing—review and editing, V.G.P., A.V.Z. and B.B.D.; visualization, V.G.P. and K.B.S.; supervision, A.V.Z. and B.B.D.; project administration, A.V.Z. and B.B.D.; funding acquisition, A.V.Z. and B.B.D. All authors have read and agreed to the published version of the manuscript.

Funding: The work was financially supported by the Russian Federation, represented by the Ministry of Science and Higher Education of the Russian Federation (agreement no. 075-15-2025-649 dated 20 August 2025).

Data Availability Statement: The raw data supporting the conclusions of this article will be made available by the authors on request.

Conflicts of Interest: The authors declare no conflicts of interest.

References

1. Wu, J.; Wang, X.; Wang, Q.; Lou, Z.; Li, S.; Zhu, Y.; Qin, L.; Wei, H. Nanomaterials with enzyme-like characteristics (nanozymes): Next-generation artificial enzymes (II). *Chem. Soc. Rev.* **2019**, *48*, 1004–1076. [CrossRef] [PubMed]
2. Feng, M.; Li, X.; Zhang, X.; Huang, Y. Recent advances in the development and analytical applications of oxidase-like nanozymes. *TrAC Trends Anal. Chem.* **2023**, *166*, 117220. [CrossRef]
3. Singh, S.; Rai, N.; Tiwari, H.; Gupta, P.; Verma, A.; Kumar, R.; Kailashiya, V.; Salvi, P.; Gautam, V. Recent Advancements in the Formulation of Nanomaterials-Based Nanozymes, Their Catalytic Activity, and Biomedical Applications. *ACS Appl. Bio Mater.* **2023**, *6*, 3577–3599. [CrossRef]
4. Ren, X.; Chen, D.; Wang, Y.; Li, H.; Zhang, Y.; Chen, H.; Li, X.; Huo, M. Nanozymes-recent development and biomedical applications. *J. Nanobiotechnol.* **2022**, *20*, 92. [CrossRef]
5. Wu, J.; Li, S.; Wei, H. Multifunctional nanozymes: Enzyme-like catalytic activity combined with magnetism and surface plasmon resonance. *Nanoscale Horiz.* **2018**, *3*, 367–382. [CrossRef]
6. Zandieh, M.; Liu, J. Nanozymes: Definition, Activity, and Mechanisms. *Adv. Mater.* **2024**, *36*, 2211041. [CrossRef]
7. Li, Y.; Liu, J. Nanozyme's catching up: Activity, specificity, reaction conditions and reaction types. *Mater. Horiz.* **2021**, *8*, 336–350. [CrossRef]
8. Zhang, R.; Yan, X.; Fan, K. Nanozymes Inspired by Natural Enzymes. *Acc. Mater. Res.* **2021**, *2*, 534–547. [CrossRef]
9. Zhang, X.; Li, G.; Chen, G.; Wu, D.; Zhou, X.; Wu, Y. Single-atom nanozymes: A rising star for biosensing and biomedicine. *Coord. Chem. Rev.* **2020**, *418*, 213376. [CrossRef]
10. Xia, Y.; Gilroy, K.D.; Peng, H.; Xia, X. Seed-Mediated Growth of Colloidal Metal Nanocrystals. *Angew. Chem. Int. Ed.* **2017**, *56*, 60–95. [CrossRef] [PubMed]
11. Xia, X.; Zhang, J.; Lu, N.; Kim, M.J.; Ghale, K.; Xu, Y.; McKenzie, E.; Liu, J.; Ye, H. Pd–Ir Core–Shell Nanocubes: A Type of Highly Efficient and Versatile Peroxidase Mimic. *ACS Nano* **2015**, *9*, 9994–10004. [CrossRef]
12. Gao, Z.; Ye, H.; Tang, D.; Tao, J.; Habibi, S.; Minerick, A.; Tang, D.; Xia, X. Platinum-Decorated Gold Nanoparticles with Dual Functionalities for Ultrasensitive Colorimetric in Vitro Diagnostics. *Nano Lett.* **2017**, *17*, 5572–5579. [CrossRef]
13. Ma, Y.; Li, W.; Cho, E.C.; Li, Z.; Yu, T.; Zeng, J.; Xie, Z.; Xia, Y. Au@Ag Core−Shell Nanocubes with Finely Tuned and Well-Controlled Sizes, Shell Thicknesses, and Optical Properties. *ACS Nano* **2010**, *4*, 6725–6734. [CrossRef] [PubMed]

14. Wang, X.; Vara, M.; Luo, M.; Huang, H.; Ruditskiy, A.; Park, J.; Bao, S.; Liu, J.; Howe, J.; Chi, M.; et al. Pd@Pt Core–Shell Concave Decahedra: A Class of Catalysts for the Oxygen Reduction Reaction with Enhanced Activity and Durability. *J. Am. Chem. Soc.* **2015**, *137*, 15036–15042. [CrossRef] [PubMed]
15. Cui, M.; Xu, B.; Wang, L. Recent advances in multi-metallic-based nanozymes for enhanced catalytic cancer therapy. *BMEMat* **2024**, *2*, e12043. [CrossRef]
16. Shen, X.; Wang, Z.; Gao, X.J.; Gao, X. Reaction Mechanisms and Kinetics of Nanozymes: Insights from Theory and Computation. *Adv. Mater.* **2024**, *36*, 2211151. [CrossRef] [PubMed]
17. Wang, W.; Cao, Q.; He, J.; Xie, Y.; Zhang, Y.; Yang, L.; Duan, M.; Wang, J.; Li, W. Palladium/Platinum/Ruthenium Trimetallic Dendritic Nanozymes Exhibiting Enhanced Peroxidase-like Activity for Signal Amplification of Lateral Flow Immunoassays. *Nano Lett.* **2024**, *27*, 8311–8319. [CrossRef]
18. He, X.; Wang, Z.; Mao, B.; Lin, H.; Jin, X.; Du, M.; Huang, B.; Xin, S.; Qu, J.; Feng, Y. Trimetallic Pt-Pd-Au alloy nanozymes for multimodal synergistic therapy to overcome deep-seated drug-resistant infections via ROS cascade ☆. *Bioact. Mater.* **2025**, *51*, 841–857. [CrossRef]
19. Zeledón, J.A.Z.; Stevens, M.B.; Gunasooriya, G.T.K.K.; Gallo, A.; Landers, A.T.; Kreider, M.E.; Hahn, C.; Nørskov, J.K.; Jaramillo, T.F. Tuning the electronic structure of Ag-Pd alloys to enhance performance for alkaline oxygen reduction. *Nat. Commun.* **2021**, *12*, 620. [CrossRef]
20. Qiao, H.; Wang, X.; Dong, Q.; Zheng, H.; Chen, G.; Hong, M.; Yang, C.-P.; Wu, M.; He, K.; Hu, L. A high-entropy phosphate catalyst for oxygen evolution reaction. *Nano Energy* **2021**, *86*, 106029. [CrossRef]
21. Zhao, Z.; Liu, H.; Gao, W.; Xue, W.; Liu, Z.; Huang, J.; Pan, X.; Huang, Y. Surface-Engineered PtNi-O Nanostructure with Record-High Performance for Electrocatalytic Hydrogen Evolution Reaction. *J. Am. Chem. Soc.* **2018**, *140*, 9046–9050. [CrossRef]
22. Wu, C.H.; Liu, C.; Su, D.; Xin, H.L.; Fang, H.-T.; Eren, B.; Zhang, S.; Murray, C.B.; Salmeron, M.B. Bimetallic synergy in cobalt–palladium nanocatalysts for CO oxidation. *Nat. Catal.* **2018**, *2*, 78–85. [CrossRef]
23. Pietrzak, M.; Ivanova, P. Bimetallic and Multimetallic Nanoparticles as Nanozymes. *Sens. Actuators B Chem.* **2021**, *336*, 129736. [CrossRef]
24. Phan-Xuan, T.; Breitung, B.; Dailey, L.A. Nanozymes for biomedical applications: Multi-metallic systems may improve activity but at the cost of higher toxicity? *WIREs Nanomed. Nanobiotechnol.* **2024**, *16*, e1981. [CrossRef]
25. Xin, Y.; Li, S.; Qian, Y.; Zhu, W.; Yuan, H.; Jiang, P.; Guo, R.; Wang, L. High-Entropy Alloys as a Platform for Catalysis: Progress, Challenges, and Opportunities. *ACS Catal.* **2020**, *10*, 11280–11306. [CrossRef]
26. Wang, X.; Shu, C.; Wang, G.; Han, P.; Zheng, L.; Xu, L.; Chen, Y. Recent progress of noble metal-based nanozymes: Structural engineering and biomedical applications. *Nanoscale* **2025**, *17*, 10557–10580. [CrossRef] [PubMed]
27. Zhang, Y.; Liu, B.; Zhang, H. Preparation of nanocube PtRhIr nanozyme and its application in ultrasensitive lateral flow immunoassay. *Mater. Lett.* **2025**, *385*, 138123. [CrossRef]
28. Gao, W.; Eastwood, H.; Xia, X. Peroxidase mimics of platinum-group metals for in vitro diagnostics: Opportunities and challenges. *J. Mater. Chem. B* **2023**, *11*, 8404–8410. [CrossRef] [PubMed]
29. Phan-xuan, T.; Schweidler, S.; Hirte, S.; Schu, M.; Lin, L.; Khandelwal, A.; Wang, K.; Schu, J.; Reischl, M.; Ku, C.; et al. Using the High-Entropy Approach to Obtain Multimetal Oxide Nanozymes: Library Synthesis, In Silico Structure—Activity, and Immunoassay Performance. *ACS Nano* **2024**, *18*, 19024–19037. [CrossRef]
30. Tang, Z.; Yeo, B.C.; Han, S.S.; Lee, T.J.; Bhang, S.H.; Kim, W.S.; Yu, T. Facile aqueous-phase synthesis of Ag–Cu–Pt–Pd quadrometallic nanoparticles. *Nano Converg.* **2019**, *6*, 38. [CrossRef]
31. Frens, G. Controlled Nucleation for the Regulation of the Particle Size in Monodisperse Gold Suspensions. *Nat. Phys. Sci.* **1973**, *241*, 20–22. [CrossRef]
32. Panferov, V.G.; Byzova, N.A.; Zherdev, A.V.; Dzantiev, B.B. Peroxidase-mimicking nanozyme with surface-dispersed Pt atoms for the colorimetric lateral flow immunoassay of C-reactive protein. *Microchim. Acta* **2021**, *188*, 309. [CrossRef] [PubMed]
33. Jiang, B.; Duan, D.; Gao, L.; Zhou, M.; Fan, K.; Tang, Y.; Xi, J.; Bi, Y.; Tong, Z.; Gao, G.F.; et al. Standardized assays for determining the catalytic activity and kinetics of peroxidase-like nanozymes. *Nat. Protoc.* **2018**, *13*, 1506–1520. [CrossRef]
34. Xia, X.; Wang, Y.; Ruditskiy, A.; Xia, Y. 25th Anniversary Article: Galvanic Replacement: A Simple and Versatile Route to Hollow Nanostructures with Tunable and Well-Controlled Properties. *Adv. Mater.* **2013**, *25*, 6313–6333. [CrossRef]
35. Li, J.; Liu, J.; Yang, Y.; Qin, D. Bifunctional Ag@Pd-Ag Nanocubes for Highly Sensitive Monitoring of Catalytic Reactions by Surface-Enhanced Raman Spectroscopy. *J. Am. Chem. Soc.* **2015**, *137*, 7039–7042. [CrossRef] [PubMed]
36. Liu, X.; Astruc, D. From Galvanic to Anti-Galvanic Synthesis of Bimetallic Nanoparticles and Applications in Catalysis, Sensing, and Materials Science. *Adv. Mater.* **2017**, *29*, 1605305. [CrossRef] [PubMed]
37. Yang, T.; Ahn, J.; Shi, S.; Wang, P.; Gao, R.; Qin, D. Noble-Metal Nanoframes and Their Catalytic Applications. *Chem. Rev.* **2021**, *121*, 796–833. [CrossRef]
38. Merkoçi, F.; Patarroyo, J.; Russo, L.; Piella, J.; Genç, A.; Arbiol, J.; Bastús, N.G.; Puntes, V. Understanding galvanic replacement reactions: The case of Pt and Ag. *Mater. Today Adv.* **2020**, *5*, 100037. [CrossRef]

39. Li, K.; Liu, G.; Zhang, S.; Dai, Y.; Ghafoor, S.; Huang, W.; Zu, Z.; Lu, Y. A porous Au-Ag hybrid nanoparticle array with broadband absorption and high-density hotspots for stable SERS analysis. *Nanoscale* **2019**, *11*, 9587–9592. [CrossRef]
40. Zhang, W.; Yang, J.; Lu, X. Tailoring Galvanic Replacement Reaction for the Preparation of Pt/Ag Bimetallic Hollow Nanostructures with Controlled Number of Voids. *ACS Nano* **2012**, *6*, 7397–7405. [CrossRef]
41. Sun, Y.; Xia, Y. Mechanistic Study on the Replacement Reaction between Silver Nanostructures and Chloroauric Acid in Aqueous Medium. *J. Am. Chem. Soc.* **2004**, *126*, 3892–3901. [CrossRef]
42. Sun, Y.; Mayers, B.T.; Xia, Y. Template-Engaged Replacement Reaction: A One-Step Approach to the Large-Scale Synthesis of Metal Nanostructures with Hollow Interiors. *Nano Lett.* **2002**, *2*, 481–485. [CrossRef]
43. Khlebtsov, N.G.; Dykman, L.A. Optical properties and biomedical applications of plasmonic nanoparticles. *J. Quant. Spectrosc. Radiat. Transf.* **2010**, *111*, 1–35. [CrossRef]
44. Panferov, V.G.; Liu, J. Optical and Catalytic Properties of Nanozymes for Colorimetric Biosensors: Advantages, Limitations, and Perspectives. *Adv. Opt. Mater.* **2024**, *12*, 2401318. [CrossRef]
45. Bai, T.; Wang, L.; Wang, M.; Zhu, Y.; Li, W.; Guo, Z.; Zhang, Y. Strategic synthesis of trimetallic Au@Ag–Pt nanorattles for ultrasensitive colorimetric detection in lateral flow immunoassay. *Biosens. Bioelectron.* **2022**, *208*, 114218. [CrossRef]
46. Panferov, V.G.; Liu, J. Nanozyme catalysis in a crowded environment: The impact of diffusion and surface shielding. *Nano Res.* **2024**, *17*, 5795–5800. [CrossRef]
47. Panferov, V.G.; Zhang, X.; Wong, K.; Lee, J.H.; Liu, J. Biomedical Applications of Nanozymes: An Enzymology Perspective. *Angew. Chem. Int. Ed.* **2025**, *64*, e202512409. [CrossRef] [PubMed]
48. Garcia-Peiro, J.I.; Bonet-Aleta, J.; Tamayo-Fraile, M.L.; Hueso, J.L.; Santamaria, J. Platinum-based nanodendrites as glucose oxidase-mimicking surrogates. *Nanoscale* **2023**, *15*, 14399–14408. [CrossRef]
49. Wei, H.; Gao, L.; Fan, K.; Liu, J.; He, J.; Qu, X.; Dong, S.; Wang, E.; Yan, X. Nanozymes: A clear definition with fuzzy edges. *Nano Today* **2021**, *40*, 101269. [CrossRef]
50. Thangudu, S.; Su, C.-H. Peroxidase Mimetic Nanozymes in Cancer Phototherapy: Progress and Perspectives. *Biomolecules* **2021**, *11*, 1015. [CrossRef]
51. Singh, N.; Sherin, G.R.; Mugesh, G. Antioxidant and Prooxidant Nanozymes: From Cellular Redox Regulation to Next-Generation Therapeutics. *Angew. Chem. Int. Ed.* **2023**, *62*, e202301232. [CrossRef]
52. Yuan, B.; Chou, H.-L.; Peng, Y.-K. Disclosing the Origin of Transition Metal Oxides as Peroxidase (and Catalase) Mimetics. *ACS Appl. Mater. Interfaces* **2022**, *14*, 22728–22736. [CrossRef] [PubMed]
53. Ai, Y.; Wang, Z.; Shi, W.; Jia, X.; Cui, M.; Sun, H.; Ren, F.; He, M.; Liang, Q. Atomic-Level High-Entropy Nanozymes Enable Remarkable Endogenous Targeted Catalysis and Enhancing Tumor Photothermal Therapy. *Adv. Mater.* **2025**, *37*, 2502322. [CrossRef]
54. Zandieh, M.; Liu, J. Nanozyme Catalytic Turnover and Self-Limited Reactions. *ACS Nano* **2021**, *15*, 15645–15655. [CrossRef]
55. Akbarzadeh, H.; Mehrjouei, E.; Abbaspour, M.; Salemi, S.; Yaghoubi, H.; Kamrani, M. Thermal behavior of different types of Au–Pt–Pd nanoparticles: Dumbbell-like, three-shell, core-shell, and random-alloy. *Mater. Chem. Phys.* **2023**, *294*, 126955. [CrossRef]
56. Wei, S.; Zhang, C.; Zhang, S. Harnessing Proton as a Performance Amplifier in Nanozyme Catalysis for Ultrasensitive Detection. *Adv. Funct. Mater.* **2025**, e14080. [CrossRef]
57. Panferov, V.G.; D'Abruzzo, N.; Byzova, N.A.; Liu, J. Nanozyme-Linked Immunosorbent Assays: A Kinetic Perspective. *Langmuir* **2025**, *41*, 29924–29932. [CrossRef]
58. Wu, J.; Qin, K.; Yuan, D.; Tan, J.; Qin, L.; Zhang, X.; Wei, H. Rational Design of Au@Pt Multibranched Nanostructures as Bifunctional Nanozymes. *ACS Appl. Mater. Interfaces* **2018**, *10*, 12954–12959. [CrossRef] [PubMed]
59. Sun, Y.; Wiley, B.; Li, Z.Y.; Xia, Y. Synthesis and optical properties of nanorattles and multiple-walled nanoshells/nanotubes made of metal alloys. *J. Am. Chem. Soc.* **2004**, *126*, 9399–9406. [CrossRef] [PubMed]
60. Hughes, A.E.; Haque, N.; Northey, S.A.; Giddey, S. Platinum Group Metals: A Review of Resources, Production and Usage with a Focus on Catalysts. *Resources* **2021**, *10*, 93. [CrossRef]
61. Nagendran, V.; Goveas, L.C.; Vinayagam, R.; Varadavenkatesan, T.; Selvaraj, R. Nanozymes in environmental remediation: A bibliometric and comprehensive review of their oxidoreductase-mimicking capabilities. *Microchem. J.* **2024**, *207*, 111748. [CrossRef]
62. Panferov, V.G.; Zhang, W.; D'aBruzzo, N.; Wang, S.; Liu, J. Kinetic Profiling of Oxidoreductase-Mimicking Nanozymes: Impact of Multiple Activities, Chemical Transformations, and Colloidal Stability. *ACS Nano* **2024**, *18*, 34870–34883. [CrossRef] [PubMed]
63. Sun, B.; Panferov, V.; Guo, X.; Xiong, J.; Zhang, S.; Qin, L.; Yin, C.; Wang, X.; Liu, C.; Han, K.; et al. A novel triple-signal biosensor based on ZrFe-MOF@PtNPs for ultrasensitive aflatoxins detection. *Biosens. Bioelectron.* **2024**, *267*, 116797. [CrossRef]
64. Niu, X.; Shi, Q.; Zhu, W.; Liu, D.; Tian, H.; Fu, S.; Cheng, N.; Li, S.; Smith, J.N.; Du, D.; et al. Unprecedented peroxidase-mimicking activity of single-atom nanozyme with atomically dispersed Fe–Nx moieties hosted by MOF derived porous carbon. *Biosens. Bioelectron.* **2019**, *142*, 111495. [CrossRef] [PubMed]

65. Panferov, V.G.; Safenkova, I.V.; Zherdev, A.V.; Dzantiev, B.B. Urchin peroxidase-mimicking Au@Pt nanoparticles as a label in lateral flow immunoassay: Impact of nanoparticle composition on detection limit of Clavibacter michiganensis. *Microchim. Acta* **2020**, *187*, 1–10. [CrossRef]
66. Chen, S.; Yu, Z.; Wang, Y.; Tang, J.; Zeng, Y.; Liu, X.; Tang, D. Block-Polymer-Restricted Sub-nanometer Pt Nanoclusters Nanozyme-Enhanced Immunoassay for Monitoring of Cardiac Troponin I. *Anal. Chem.* **2023**, *95*, 14494–14501. [CrossRef]
67. Fan, H.; Zheng, J.; Xie, J.; Liu, J.; Gao, X.; Yan, X.; Fan, K.; Gao, L. Surface Ligand Engineering Ruthenium Nanozyme Superior to Horseradish Peroxidase for Enhanced Immunoassay. *Adv. Mater.* **2023**, *36*, e2300387. [CrossRef]
68. Jiao, L.; Wu, J.; Zhong, H.; Zhang, Y.; Xu, W.; Wu, Y.; Chen, Y.; Yan, H.; Zhang, Q.; Gu, W.; et al. Densely Isolated FeN_4 Sites for Peroxidase Mimicking. *ACS Catal.* **2020**, *10*, 6422–6429. [CrossRef]
69. Zhao, C.; Xiong, C.; Liu, X.; Qiao, M.; Li, Z.; Yuan, T.; Wang, J.; Qu, Y.; Wang, X.; Zhou, F.; et al. Unraveling the enzyme-like activity of heterogeneous single atom catalyst. *Chem. Commun.* **2019**, *55*, 2285–2288. [CrossRef]
70. Hong, J.; Guo, Z.; Duan, D.; Zhang, Y.; Chen, X.; Li, Y.; Tu, Z.; Feng, L.; Chen, L.; Yan, X.; et al. Highly sensitive nanozyme strip: An effective tool for forensic material evidence identification. *Nano Res.* **2023**, *17*, 1785–1791. [CrossRef]
71. Huang, Y.; Ding, Z.; Li, Y.; Xi, F.; Liu, J. Magnetic Nanozyme Based on Loading Nitrogen-Doped Carbon Dots on Mesoporous Fe_3O_4 Nanoparticles for the Colorimetric Detection of Glucose. *Molecules* **2023**, *28*, 4573. [CrossRef] [PubMed]
72. Liu, D.; Ju, C.; Han, C.; Shi, R.; Chen, X.; Duan, D.; Yan, J.; Yan, X. Nanozyme chemiluminescence paper test for rapid and sensitive detection of SARS-CoV-2 antigen. *Biosens. Bioelectron.* **2021**, *173*, 112817. [CrossRef] [PubMed]
73. Meng, X.; Zou, S.; Li, D.; He, J.; Fang, L.; Wang, H.; Yan, X.; Duan, D.; Gao, L. Nanozyme-strip for rapid and ultrasensitive nucleic acid detection of SARS-CoV-2. *Biosens. Bioelectron.* **2022**, *217*, 114739. [CrossRef]
74. Wang, Y.; Feng, Q.; Liu, M.; Xue, L.; Wang, G.; Zhang, S.; Hu, W. N, P, S Codoped Carbon Nanozymes with Enhanced Peroxidase-like Activity and Binding Affinity for Total Antioxidant Capacity Assay. *ACS Appl. Nano Mater.* **2023**, *6*, 23303–23312. [CrossRef]
75. Dong, H.; Du, W.; Dong, J.; Che, R.; Kong, F.; Cheng, W.; Ma, M.; Gu, N.; Zhang, Y. Depletable peroxidase-like activity of Fe3O4 nanozymes accompanied with separate migration of electrons and iron ions. *Nat. Commun.* **2022**, *13*, 1–11. [CrossRef] [PubMed]
76. Jiao, L.; Xu, W.; Zhang, Y.; Wu, Y.; Gu, W.; Ge, X.; Chen, B.; Zhu, C.; Guo, S. Boron-doped Fe-N-C single-atom nanozymes specifically boost peroxidase-like activity. *Nano Today* **2020**, *35*, 100971. [CrossRef]
77. Khramtsov, P.; Kropaneva, M.; Minin, A.; Bochkova, M.; Timganova, V.; Maximov, A.; Puzik, A.; Zamorina, S.; Rayev, M. Prussian Blue Nanozymes with Enhanced Catalytic Activity: Size Tuning and Application in ELISA-like Immunoassay. *Nanomaterials* **2022**, *12*, 1630. [CrossRef]
78. Luo, Y.; Luo, H.; Zou, S.; Jiang, J.; Duan, D.; Chen, L.; Gao, L. An In Situ Study on Nanozyme Performance to Optimize Nanozyme-Strip for Aβ Detection. *Sensors* **2023**, *23*, 3414. [CrossRef]
79. Tao, Z.; Wei, L.; Wu, S.; Duan, N.; Li, X.; Wang, Z. A colorimetric aptamer-based method for detection of cadmium using the enhanced peroxidase-like activity of Au–MoS2 nanocomposites. *Anal. Biochem.* **2020**, *608*, 113844. [CrossRef]
80. Li, S.; Zhao, F.; Yu, H.; Xu, Z.; Ali, Z.; Li, W.; Ying, Y.; Qiao, L.; Zheng, J.; Li, J.; et al. Regulating peroxidase-mimic activity of iron oxide nanozymes through size modulation: Electronic structure and specific surface area. *Rare Met.* **2025**, *44*, 6375–6387. [CrossRef]
81. Zhang, J.; Sun, B.; Zhang, M.; Su, Y.; Xu, W.; Sun, Y.; Jiang, H.; Zhou, N.; Shen, J.; Wu, F. Modulating the local coordination environment of cobalt single-atomic nanozymes for enhanced catalytic therapy against bacteria. *Acta Biomater.* **2023**, *164*, 563–576. [CrossRef]
82. Jia, Z.; Lv, X.; Hou, Y.; Wang, K.; Ren, F.; Xu, D.; Wang, Q.; Fan, K.; Xie, C.; Lu, X. Mussel-inspired nanozyme catalyzed conductive and self-setting hydrogel for adhesive and antibacterial bioelectronics. *Bioact. Mater.* **2021**, *6*, 2676–2687. [CrossRef]
83. Ming, J.; Zhu, T.; Li, J.; Ye, Z.; Shi, C.; Guo, Z.; Wang, J.; Chen, X.; Zheng, N. A Novel Cascade Nanoreactor Integrating Two-Dimensional Pd-Ru Nanozyme, Uricase and Red Blood Cell Membrane for Highly Efficient Hyperuricemia Treatment. *Small* **2021**, *17*, 2103645. [CrossRef]
84. Xi, J.; Zhang, R.; Wang, L.; Xu, W.; Liang, Q.; Li, J.; Jiang, J.; Yang, Y.; Yan, X.; Fan, K.; et al. A Nanozyme-Based Artificial Peroxisome Ameliorates Hyperuricemia and Ischemic Stroke. *Adv. Funct. Mater.* **2020**, *31*. [CrossRef]
85. Ye, Z.; Fan, Y.; Zhu, T.; Cao, D.; Hu, X.; Xiang, S.; Li, J.; Guo, Z.; Chen, X.; Tan, K.; et al. Preparation of Two-Dimensional Pd@Ir Nanosheets and Application in Bacterial Infection Treatment by the Generation of Reactive Oxygen Species. *ACS Appl. Mater. Interfaces* **2022**, *14*, 23194–23205. [CrossRef] [PubMed]
86. He, S.-B.; Lin, M.-T.; Yang, L.; Noreldeen, H.A.A.; Peng, H.-P.; Deng, H.-H.; Chen, W. Protein-Assisted Osmium Nanoclusters with Intrinsic Peroxidase-like Activity and Extrinsic Antifouling Behavior. *ACS Appl. Mater. Interfaces* **2021**, *13*, 44541–44548. [CrossRef]
87. Hao, J.; Zhang, C.; Feng, C.; Wang, Q.; Liu, Z.-Y.; Li, Y.; Mu, J.; Yang, E.-C.; Wang, Y. An ultra-highly active nanozyme of Fe,N co-doped ultrathin hollow carbon framework for antibacterial application. *Chin. Chem. Lett.* **2022**, *34*, 107650. [CrossRef]

88. Wang, W.; Zhu, Y.; Zhu, X.; Zhao, Y.; Xue, Z.; Xiong, C.; Wang, Z.; Qu, Y.; Cheng, J.; Chen, M.; et al. Biocompatible Ruthenium Single-Atom Catalyst for Cascade Enzyme-Mimicking Therapy. *ACS Appl. Mater. Interfaces* **2021**, *13*, 45269–45278. [CrossRef]
89. Jiao, L.; Kang, Y.; Chen, Y.; Wu, N.; Wu, Y.; Xu, W.; Wei, X.; Wang, H.; Gu, W.; Zheng, L.; et al. Unsymmetrically coordinated single Fe-N3S1 sites mimic the function of peroxidase. *Nano Today* **2021**, *40*, 101261. [CrossRef]
90. Chen, Y.; Jiao, L.; Yan, H.; Xu, W.; Wu, Y.; Zheng, L.; Gu, W.; Zhu, C. Fe–N–C Single-Atom Catalyst Coupling with Pt Clusters Boosts Peroxidase-like Activity for Cascade-Amplified Colorimetric Immunoassay. *Anal. Chem.* **2021**, *93*, 12353–12359. [CrossRef] [PubMed]
91. Ji, S.; Jiang, B.; Hao, H.; Chen, Y.; Dong, J.; Mao, Y.; Zhang, Z.; Gao, R.; Chen, W.; Zhang, R.; et al. Matching the kinetics of natural enzymes with a single-atom iron nanozyme. *Nat. Catal.* **2021**, *4*, 407–417. [CrossRef]
92. Zhou, X.; Fan, C.; Tian, Q.; Han, C.; Yin, Z.; Dong, Z.; Bi, S. Trimetallic AuPtCo Nanopolyhedrons with Peroxidase- and Catalase-Like Catalytic Activity for Glow-Type Chemiluminescence Bioanalysis. *Anal. Chem.* **2021**, *94*, 847–855. [CrossRef] [PubMed]
93. Huang, L.; Zhou, Y.; Zhu, Y.; Su, H.; Yang, S.; Feng, L.; Zhao, L.; Liu, S.; Qian, K. Dual-modal nanoplatform integrated with smartphone for hierarchical diabetic detection. *Biosens. Bioelectron.* **2022**, *210*, 114254. [CrossRef] [PubMed]
94. Tang, Y.; Wu, Y.; Xu, W.; Jiao, L.; Chen, Y.; Sha, M.; Ye, H.-R.; Gu, W.; Zhu, C. Ultrathin Ruthenium Nanosheets with Crystallinity-Modulated Peroxidase-like Activity for Protein Discrimination. *Anal. Chem.* **2021**, *94*, 1022–1028. [CrossRef] [PubMed]
95. Feng, F.; Zhang, Y.; Zhang, X.; Mu, B.; Zhang, J.; Qu, W.; Tong, W.; Liang, M.; An, Q.; Guo, Z.; et al. Enhancing the peroxidase-like activity of MoS2-based nanozymes by introducing attapulgite for antibacterial application and sensitive detection of glutathione. *Nano Res.* **2024**, *17*, 7415–7426. [CrossRef]

Disclaimer/Publisher's Note: The statements, opinions and data contained in all publications are solely those of the individual author(s) and contributor(s) and not of MDPI and/or the editor(s). MDPI and/or the editor(s) disclaim responsibility for any injury to people or property resulting from any ideas, methods, instructions or products referred to in the content.